Time-dependent global sensitivity analysis with active subspaces for a lithium ion battery model

Paul G. Constantine*
Department of Applied Mathematics and Statistics
Colorado School of Mines
and
Alireza Doostan
Department of Aerospace Engineering Sciences
University of Colorado Boulder

November 2, 2022

Abstract

Renewable energy researchers use computer simulation to aid the design of lithium ion storage devices. The underlying models contain several physical input parameters that affect model predictions. Effective design and analysis must understand the sensitivity of model predictions to changes in model parameters, but global sensitivity analyses become increasingly challenging as the number of input parameters increases. Active subspaces are part of an emerging set of tools to reveal and exploit low-dimensional structures in the map from high-dimensional inputs to model outputs. We extend a linear model-based heuristic for active subspace discovery to time-dependent processes and apply the resulting technique to a lithium ion battery model. The results reveal low-dimensional structure that a designer may exploit to efficiently study the relationship between parameters and predictions.

Keywords: sufficient dimension reduction, computer experiments, uncertainty quantification

technometrics tex template (do not remove)

*We thank Dr. Mohammad Hadigol for providing us with the Li battery data set used in this work. This material is based upon (i) work of PC supported by the U.S. Department of Energy Office of Science, Office of Advanced Scientific Computing Research, Applied Mathematics program under Award Number DE-SC-0011077 and the Defense Advanced Research Projects Agency's Enabling Quantification of Uncertainty in Physical Systems and (ii) work of AD supported by the U.S. Department of Energy Office of Science, Office of Advanced Scientific Computing Research, under Award Number DE-SC0006402 and NSF grant CMMI-1454601.

1 Introduction

With $27 billion in yearly sales, lithium (Li) batteries are the most widely used rechargeable batteries in small portable electronics (e.g., laptops and cell-phones), satellite power systems, and the automotive industry (Winter and Brodd, 2004). Assemblies of several cells in series and parallel configurations are commonly used to address issues of precise energy delivery. Although Li batteries are appealing for their high energy density and high operating voltage, their usage is restricted to low-to-medium power applications, because they often have short lifetimes and safety issues.

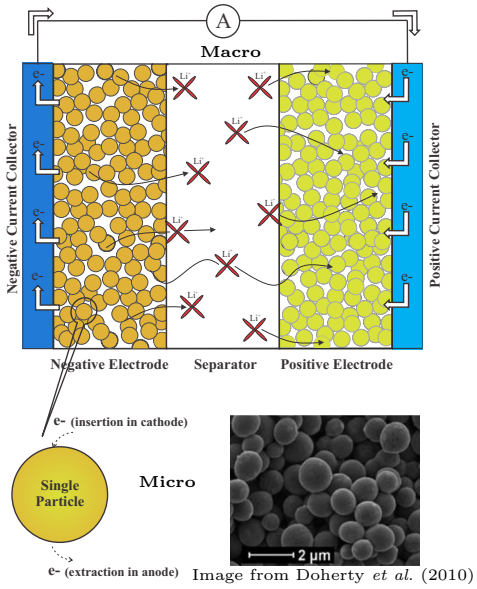

Image from Doherty *et al.* (2010)

Figure 1: Schematic of a Li battery cell identifying macro- and micro-scale models.

From a modeling perspective, an Li battery is a multi-scale and multi-physics system. The spatial length scales of interest range from the thickness of the overall cell (millimeters) to nanometer sized particles in electrode porous media (see Figure 1). Physical phenomena include transport processes, mechanical deformations and fracture, and electrochemical reactions. According to the physics, the dominant cause for the shortened lifetime of Li batteries is the chemical and mechanical degradation of the electrode particles as a consequence of electrical, chemical, and mechanical interactions during charge and discharge cycles. Accurate simulation of such phenomena—as well as their interactions—to predict battery performance is especially challenging for several reasons: (i) models contain many

input parameters that must be set based on sparse experimental data, (ii) manufactured cells vary due to inherent process variability, and (iii) several physical assumptions are needed to simplify the complex physics. One approach to address these difficulties is to develop data-driven battery models that account for various sources of uncertainty—e.g., parameter variability or simplified physics—and to quantify the impact of such uncertainties on the quantities of interest (QoIs), as recently advocated by Santhanagopalan and White (2007); Dua *et al.* (2010); Hadigol *et al.* (2015), among others. The emerging field of uncertainty quantification (UQ) studies systematic methodologies for the data-driven approach.

In the probabilistic framework for UQ that we employ, system uncertainties are represented using a set of independent random variables $\mathbf{x} \in \mathbb{R}^m$ with a joint probability density function $\rho(\mathbf{x})$, where ρ is chosen and/or derived from data and expert opinion. The system's governing, parameter-dependent equations are then stochastic, and the solution of interest $f(\mathbf{x})$ is consequently a random variable; for simplicity, we consider scalar-valued quantities of interest, $f \in \mathbb{R}$. One of UQ's main objectives is to construct an approximation of the mapping $\mathbf{x} \to f(\mathbf{x})$, for instance, using a set of input samples $\mathbf{x}_j$, $j = 1, \ldots, N$, and the corresponding QoI realizations $f(\mathbf{x}_j)$. For problems with multi-physics and/or multi-scale features, such as Li batteries, the number of random variables m needed to characterize the overall uncertainty may be large. In such cases, approximating $f(\mathbf{x})$ remains challenging due to the curse of dimensionality, where, to achieve a desired accuracy, the number of required realizations of $f(\mathbf{x})$ grows exponentially in m. To tackle this issue, several recent methods have relied on exploiting known *structures* in the mapping $\mathbf{x} \to f(\mathbf{x})$, including low-rank representations, (Doostan *et al.*, 2007; Doostan and Iaccarino, 2009; Nouy, 2010; Matthies and Zander, 2012; Hadigol *et al.*, 2014), sparse basis expansions, (Doostan and Owhadi, 2011; Blatman and Sudret, 2011; Mathelin and Gallivan, 2012; Hampton and Doostan, 2015b, 2016), and low-dimensional active subspaces, (Constantine *et al.*, 2014; Constantine, 2015; Constantine and Gleich, 2015), to name some.

In this paper, we demonstrate the existence of low-dimensional active subspaces in a multi-scale, multi-physics, electrochemical model of Li batteries, namely Newman's model (Newman and Tiedemann, 1975; Doyle *et al.*, 1993), incorporating various sources of uncertainty.

The idea behind active subspaces is to find important directions in the space of input parameters $\mathbf{x}$, not necessarily aligned with the coordinates of $\mathbf{x}$, that characterize f's average response to changes in $\mathbf{x}$. When the number of these important directions is small, $f(\mathbf{x})$ is effectively low-dimensional, and characterizations of the input/output map need fewer realizations of $f(\mathbf{x})$. We present a sensitivity analysis approach based on the active subspace to identify the input parameters whose perturbations most strongly affect two QoIs—cell capacity and voltage—in the Li battery model. Such information is particularly useful in quality control and design of battery systems for improved performance.

The rest of this manuscript is organized as follows. Section 2 introduces active subspaces for both stationary and time-dependent models, including how the subspaces generate sensitivity information for ranking input parameters. Section 3 describes the Li battery model and the associated data set based on the numerical simulations of Hadigol *et al.* (2015) that are used in this work. The results of active subspace technique applied to the battery data set are in Section 4. Finally, we summarize our findings and conclusions in Section 5.

2 Active subspaces

2.1 Stationary models

We present the methodology for an abstract deterministic function of several parameters $f(\mathbf{x})$, the physical model's QoI, and we follow the presentation in Constantine (2015). Let the probability density function of $\mathbf{x}$, $\rho(\mathbf{x})$, be strictly positive on parameter regimes of interest, and assume that ρ is such that (i) the mean of $\mathbf{x}$ is zero and (ii) each component of $\mathbf{x}$ varies independently within the same range.[1] Assume that f is differentiable with gradient vector $\nabla f(\mathbf{x}) \in \mathbb{R}^m$, and assume that f and its partial derivatives are square-integrable with respect to ρ.

Define the $m \times m$ symmetric positive semidefinite matrix $\boldsymbol{C}$ as

$$\boldsymbol{C} \;=\; \int \nabla f(\mathbf{x})\, \nabla f(\mathbf{x})^T\, \rho(\mathbf{x})\, d\mathbf{x}. \tag{1}$$

[1] A given parameter space with independent components can be shifted and scaled to satisfy these assumptions.

This matrix admits a real eigenvalue decomposition,

$$\boldsymbol{C} = \boldsymbol{W}\Lambda\boldsymbol{W}^T, \qquad \boldsymbol{W} = \begin{bmatrix} \mathbf{w}_1 & \cdots & \mathbf{w}_m \end{bmatrix}, \qquad \Lambda = \begin{bmatrix} \lambda_1 & & \\ & \ddots & \\ & & \lambda_m \end{bmatrix}, \tag{2}$$

where the eigenvalues are in descending order. The eigenpairs are functionals of $f(\mathbf{x})$, and they reveal important properties. Note that

$$\lambda_i \;=\; \mathbf{w}_i^T \boldsymbol{C} \mathbf{w}_i \;=\; \int \left(\nabla f(\mathbf{x})^T \mathbf{w}_i\right)^2 \rho(\mathbf{x})\, d\mathbf{x}, \quad i = 1, \ldots, m. \tag{3}$$

In words, the ith eigenvalue is the average squared directional derivative of f along the eigenvector $\mathbf{w}_i$. Thus, $\lambda_i = 0$ if and only if f is constant along $\mathbf{w}_i$. Moreover, if λ_i is relatively small, then perturbations to $\mathbf{x}$ along $\mathbf{w}_i$ change f relatively little, on average, compared to perturbations to $\mathbf{x}$ along $\mathbf{w}_j$ when $\lambda_j > \lambda_i$. Suppose that $\lambda_n > \lambda_{n+1}$ for some $n < m$. Then we can partition the eigenpairs as

$$\Lambda = \begin{bmatrix} \Lambda_1 & \\ & \Lambda_2 \end{bmatrix}, \qquad \boldsymbol{W} = \begin{bmatrix} \boldsymbol{W}_1 & \boldsymbol{W}_2 \end{bmatrix}, \tag{4}$$

where $\Lambda_1 = \mathrm{diag}(\lambda_1, \ldots, \lambda_n)$, and $\boldsymbol{W}_1$ contains the corresponding eigenvectors. The active subspace is the span of the columns of $\boldsymbol{W}_1$. If the eigenvalues $\lambda_{n+1}, \ldots, \lambda_m$ are small, then f likely varies relatively little along the column span of $\boldsymbol{W}_2$. In this case, we can justifiably approximate

$$f(\mathbf{x}) \;\approx\; g(\boldsymbol{W}_1^T \mathbf{x}), \tag{5}$$

where $g : \mathbb{R}^n \to \mathbb{R}$. The right hand side $g(\boldsymbol{W}_1^T \mathbf{x})$ is called a *ridge function* (Pinkus, 2015), and it is constant along the column span of $\boldsymbol{W}_2$. For details on the active subspace-based ridge approximation (5), see Constantine (2015, Chapter 4) and Constantine *et al.* (2014).

The simplest construction for g is as follows. Suppose we have computed an estimate $\hat{\boldsymbol{W}}_1$ of $\boldsymbol{W}_1$, and suppose we have function evaluations $f_j = f(\mathbf{x}_j)$ for $\mathbf{x}_j$'s in f's domain with $j = 1, \ldots, N$. In other words, we have run our computer model N times with inputs $\mathbf{x}_j$. Then the function $g = g(\mathbf{y})$ can be constructed from the pairs $(f_j, \mathbf{y}_j)$, where $\mathbf{y}_j = \hat{\boldsymbol{W}}_1^T \mathbf{x}_j$, using multivariate splines, polynomials, etc. This construction is in $n < m$ variables, so a budget of N evaluations permits a higher order approximation along the relatively important directions in the input parameter space than a construction in all m variables.

The low-dimensional model (5) requires an estimate of $\boldsymbol{W}_1$. If the gradient $\nabla f(\mathbf{x})$ is available as a subroutine in the simulation code (e.g., via an adjoint solution or algorithmic differentiation (Griewank, 2000)), then one strategy is to estimate the entries of $\boldsymbol{C}$ from (1) with a numerical integration rule and compute the numerical estimate's eigenpairs. If gradients are not available and evaluations of $f(\mathbf{x})$ are cheap enough, then a similar strategy may be employed with finite difference approximations. Constantine and Gleich (2015) and Constantine (2015, Chapter 3) analyze these strategies using simple Monte Carlo as the numerical integration method. However, many simulation codes—including the present battery simulation—do not have gradient capabilities, and the evaluations are too expensive to compute with finite differences. Therefore, we use a heuristic based on a linear model of $f(\mathbf{x})$.

Suppose that $f(\mathbf{x})$ can be approximated by a linear function of $\mathbf{x}$, and f's gradient can be approximated by a constant vector,

$$f(\mathbf{x}) \approx a + \mathbf{a}^T\mathbf{x}, \qquad \nabla f(\mathbf{x}) \approx \mathbf{a}. \tag{6}$$

In this case, $\boldsymbol{C}$'s eigendecomposition can be estimated as

$$\boldsymbol{C} \;\approx\; \int \mathbf{a}\,\mathbf{a}^T\,\rho(\mathbf{x})\,d\mathbf{x} \;=\; \mathbf{a}\,\mathbf{a}^T \;=\; \mathbf{w}\,\lambda\,\mathbf{w}^T, \tag{7}$$

where $\lambda = \|\mathbf{a}\|^2$ and $\mathbf{w} = \mathbf{a}/\|\mathbf{a}\|$. The active subspace is approximated by the span of $\mathbf{w}$—i.e., a one-dimensional subspace. We can compute $\mathbf{w}$ given a set of model evaluations with Algorithm 1.

Algorithm 1 is the same as Algorithm 1.3 in Constantine (2015, Chapter 1), and it is closely related to the ordinary least squares method for estimating a dimension reduction subspace in statistical regression—often dubbed *sufficient dimension reduction* (Li and Duan, 1989; Cook, 1998). The main difference between Algorithm 1 and the ordinary least squares method in sufficient dimension reduction is the problem setup and interpretation of results. A regression problem contains noise in the data that is modeled with a random variable or process. In other words, the f_j's in Algorithm 1 would be corrupted by random noise. In contrast, computer simulations are deterministic functions, so deterministic approximation (i.e., curve fitting) is more appropriate. Algorithm 1—and active subspaces, more broadly—seeks a low-dimensional parameterization for deterministic functions of several variables.

Algorithm 1 Estimate a one-dimensional active subspace with a global linear model

Given $N > m$:

1. For j from 1 to N, draw $\mathbf{x}_j$ independently according to $\rho(\mathbf{x})$, and compute $f_j = f(\mathbf{x}_j)$.
2. Compute $a^* \in \mathbb{R}$ and $\mathbf{a}^* \in \mathbb{R}^m$ as minimizers of

$$\underset{a,\mathbf{a}}{\text{minimize}} \quad \sum_{j=1}^{N} \left(f_j - (a + \mathbf{a}^T \mathbf{x}_j)\right)^2. \tag{8}$$

3. Let

$$\mathbf{w} \;=\; \mathbf{a}^* \,/\, \|\mathbf{a}^*\|, \tag{9}$$

where $\|\cdot\|$ is the Euclidean norm.

We emphasize that the goal of Algorithm 1 is to produce a single vector that identifies an important direction in the space of f's inputs. Approximating f with a linear model of $\mathbf{x}$ is not the goal.

We can easily validate the presence of a one-dimensional active subspace defined by $\mathbf{w}$ with a *summary plot*. Summary plots were developed in the context of sufficient dimension reduction for statistical regression (Cook, 1998). In the current setting, a summary plot is a scatter plot of $\mathbf{w}^T\mathbf{x}_j$ versus f_j, where $(\mathbf{x}_j, f_j)$ are the input/output pairs used to compute $\mathbf{w}$ in Algorithm 1. The summary plot may reveal a relationship between a particular linear combination of the inputs, $\mathbf{w}^T\mathbf{x}$, and the simulation model's output f. If the points in the scatter plot reveal a functional relationship, then the ridge approximation (5) with $\boldsymbol{W}_1 = \mathbf{w}$ is a good approximation to $f(\mathbf{x})$. If the points in the scatter plot do not reveal a functional relationship, then the model (5) with $\boldsymbol{W}_1 = \mathbf{w}$ may not be appropriate.

If the functional relationship is present, then the components of $\mathbf{w}$ provide sensitivity information. The normalization in (9) implies that each component is between -1 and 1. A component with a relatively large magnitude indicates that the corresponding parameter is important in defining the important subspace. Oftentimes in practice, the eigenvector components with large magnitudes correspond to parameters with relatively large standard sensitivity metrics, e.g., Sobol indices (Constantine *et al.*, 2015a; Diaz and Constantine, 2015). Moreover, if the functional relationship in the summary plot is monotonic—i.e., f

appears to be an increasing or decreasing function of $\mathbf{w}^T\mathbf{x}$—then the sign of each eigenvector component reveals how f changes in response to changes in the corresponding parameter. For example, assume that f is an increasing function of $\mathbf{w}^T\mathbf{x}$. And assume that $\mathbf{w}$'s first component is negative with a relatively large magnitude. Then, on average, a positive perturbation to x_1 decreases f. Note that the signs should be treated relative to the trend in the summary plot.

In Section 4, we apply Algorithm 1 to a Li battery model and create summary plots that give insight into the relationship between model's inputs and its outputs. However, the quantity of interest in this model also depends on a notion of time. We next extend the active subspace and ridge approximation to time-dependent quantities of interest.

2.2 Time-dependent models

Suppose that the quantity of interest depends on parameters $\mathbf{x} \in \mathbb{R}^m$ and another independent coordinate $t \in \mathbb{R}$, which we may interpret as time. In other words, $f = f(\mathbf{x}, t)$ is a parameter dependent temporal process. There are several ways to construct an active subspace for such a process. We could assume a finite time interval of interest $t \in [0, T]$ and treat t as another parameter. The extended version of $\boldsymbol{C}$ from (1) becomes

$$\boldsymbol{C} \;=\; \frac{1}{T}\int \left(\int \begin{bmatrix} f_t(\mathbf{x},t)^2 & f_t(\mathbf{x},t)\,\nabla f(\mathbf{x},t)^T \\ f_t(\mathbf{x},t)\,\nabla f(\mathbf{x}) & \nabla f(\mathbf{x},t)\,\nabla f(\mathbf{x},t)^T \end{bmatrix} \rho(\mathbf{x})\, d\mathbf{x} \right) dt, \tag{10}$$

where $f_t(\mathbf{x}, t)$ is the partial derivative of f with respect to t. Note that $\boldsymbol{C}$ from (10) admits a block structure,

$$\boldsymbol{C} \;=\; \begin{bmatrix} a & \mathbf{b}^T \\ \mathbf{b} & \boldsymbol{D} \end{bmatrix}, \quad a \in \mathbb{R}, \;\; \mathbf{b} \in \mathbb{R}^m, \;\; \boldsymbol{D} \in \mathbb{R}^{m\times m}, \tag{11}$$

where the blocks are apparent when comparing (10) to (11). We could construct a global subspace of $\mathbb{R}^m$ using the eigenvectors of the lower right block $\boldsymbol{D}$, which is symmetric and positive semidefinite. This would be equivalent to averaging a time dependent analog of $\boldsymbol{C}$ from (1) over the time interval and computing its eigenvectors. Alternatively, we could construct a global subspace from the Schur complement of (11),

$$\boldsymbol{C}_S \;=\; \boldsymbol{D} - \frac{1}{a}\,\mathbf{b}\,\mathbf{b}^T \;\in\; \mathbb{R}^{m\times m}. \tag{12}$$

We are currently examining the merits and drawbacks of each of these approaches for generic processes. We apply neither approach to the current Li battery model.

Another approach is to treat $\boldsymbol{C}$ from (1) as a matrix whose elements depend on t, i.e.,

$$\boldsymbol{C}(t) \;=\; \int \nabla f(\mathbf{x},t)\,\nabla f(\mathbf{x},t)^T\,\rho(\mathbf{x})\,d\mathbf{x} \;=\; \boldsymbol{W}(t)\,\Lambda(t)\,\boldsymbol{W}(t)^T, \tag{13}$$

where the eigendecomposition is computed independently for each t. Spectral decompositions of parameter dependent linear operators are well studied; see Kato (1966) for a complete treatment. We simplify the mathematics dramatically by considering a finite collection of points $t_k \in [0,T]$ with $k = 1,\ldots,P$. In effect, each of the P sets of m eigenpairs is indexed by k. Loudon and Pankavich (2016) use this approach to study the time dependent active subspace of a quantity of interest from a dynamical system model of HIV infection. The eigenvalues at time t_k indicate low-dimensional structure in the map from inputs to output at t_k, so one can study how that structure changes over time.

Similarly, we can use the linear model-based heuristic from Algorithm 1 at each t_k, and we can create summary plots for each t_k. The result is an animation (one summary plot for each t_k) that reveals how well a one-dimensional subspace—defined by $\mathbf{w}_k = \mathbf{w}(t_k)$ from Algorithm 1 at each t_k—captures the relationship between inputs and outputs over the time range defined by $t_1,\ldots,t_P$. If the summary plots reveal univariate trends, then the components of $\mathbf{w}_k$ can be plotted versus t_k to study the sensitivity of f with respect to $\mathbf{x}$'s components over time. A dramatic change in sensitivities may reveal a transition between physical regimes of a system.

2.3 Assessing uncertainty in the active subspace

Algorithm 1 begins with pairs $(\mathbf{x}_j, f_j)$. The $\mathbf{x}_j$'s are typically chosen according to design-of-experiments criteria, and some criteria lead to random designs. For example, simple Monte Carlo draws each $\mathbf{x}_j$ independently according to the given density $\rho(\mathbf{x})$. With random designs, it is natural to ask how robust the vector $\mathbf{w}$ from (9) is to the randomness. Practical uncertainty estimates are very difficult to derive for general nonlinear $f(\mathbf{x})$'s. We apply a nonparametric bootstrap (Efron and Tibshirani, 1994) as a heuristic to assess the uncertainty in the vector $\mathbf{w}$ computed from Algorithm 1. In particular, we can compute

the bootstrap standard error for each component of $\mathbf{w}$ by following the standard sampling-with-replacement recipe. See Efron and Tibshirani (1994, Chapter 7) for a related example applying the bootstrap to linear regression coefficients. We note that the interpretation of the standard error is not the same as in the statistical estimation, since the function values f_j are not corrupted by random noise. Nevertheless, a large bootstrap standard error may indicate (i) the data are not sufficient to compute $\mathbf{w}$ or (ii) the relationship between $\mathbf{x}$ and $f(\mathbf{x})$ cannot be summarized with one linear combination of $\mathbf{x}$.

In the time dependent case, we can plot the bootstrap standard errors at each t_k to see how they change over time. A large change from one point in time to the next may reveal that adequacy of the one-dimension subspace for capturing the relationship between $\mathbf{x}$ and f also changes. Such information may yield insight into the model's relationship between inputs and outputs.

Constantine and Gleich (2015) propose the bootstrap as a heuristic to assess uncertainty in estimates of the active subspace. Constantine *et al.* (2015b) use the bootstrap to assess uncertainty in the components $\mathbf{w}$ from Algorithm 1 for analyzing parameter dependence in a numerical model of a scramjet-powered vehicle.

2.4 Advantages and limitations

Executing Algorithm 1 and producing the summary plot is remarkably cheap. All that is needed is to fit a linear model of $f(\mathbf{x})$; recall that $\mathbf{x}$ has m components. From a linear algebra perspective, this can be accomplished with $N = m + 1$ runs if f is a linear function of $\mathbf{x}$—since the components of $\mathbf{x}$ are assumed independent. However, there is no reason to think that the quantity of interest from a complex physical simulation is exactly linear—even if it can be well approximated by a linear model. Therefore, we advise oversampling—i.e., choosing $N > m + 1$. Recent work by Hampton and Doostan (2015a) in deterministic least-squares approximation with random evaluations shows that choosing $N = \mathcal{O}(m)$ produces a linear model that behaves like the best linear approximation in the continuous, mean-squared sense.

The proper way to think of the heuristic from Algorithm 1 and its associated summary plot is as a cheap test for a particular type of low-dimensional structure, namely $f(\mathbf{x}) \approx$

$g(\mathbf{w}^T\mathbf{x})$ for $g : \mathbb{R} \to \mathbb{R}$. Similar to hypothesis tests, the test may return a false positive or a false negative. However, since the data is not corrupted by random noise, the formalism for regression hypothesis testing is not appropriate. In other words, the lack of randomness in the function evaluations implies that hypothesis tests do not have a statistically valid interpretation. Instead, we must consider the conditions that might lead to an incorrect conclusion or inconclusive results about the presence of the low-dimensional structure.

Assume that the summary plot suggests a functional relationship between the active variable $\mathbf{w}^T\mathbf{x}$ and the output $f(\mathbf{x})$. The summary plot is equivalent to viewing the relationship between $\mathbf{x}$ and $f(\mathbf{x})$ from one off-axis perspective defined by $\mathbf{w}$. This view projects the m-dimensional input space to a one-dimensional interval. Input values that appear to be close in the one-dimensional interval may be very far apart in the m-dimensional space. More precisely, for two inputs $\mathbf{x}_1$ and $\mathbf{x}_2$, $|\mathbf{w}^T\mathbf{x}_1 - \mathbf{w}^T\mathbf{x}_2|$ may be small when $\|\mathbf{x}_1 - \mathbf{x}_2\|$ is large. If f varies dramatically in a small region of the input space, then it is possible that sparsely sampled input points[2] used to construct the linear model and produce the summary plot missed the small region of dramatic variability. Resolving the region of variability (assuming sufficient sampling were possible) might change the conclusions from summary plot. In other words, this is a false positive. One way to test for this error is to compute an independent testing set and see if it satisfies the perceived functional relationship. However, any testing set short of densely sampling the m dimensional input space may produce the same false positive. In practice, we have never experienced such a false positive. We suspect this is because many physical models have outputs that vary smoothly with changes in the inputs; in other words, the dramatic variation that might lead to a false positive seems largely absent from physics-based simulation models.

Assume that the summary plot does not suggest a functional relationship between $\mathbf{w}^T\mathbf{x}$ and $f(\mathbf{x})$. In other words, the plot of $\mathbf{w}^T\mathbf{x}_j$ versus f_j looks like a collection of random points. There are three possible explanations for this. First, $f(\mathbf{x})$ might be a highly nonlinear function of $\mathbf{w}^T\mathbf{x}$, and N evaluations is not sufficient to estimate $\mathbf{w}$. The curious reader can see this phenomena on the test function $f(\mathbf{x}) = \exp(\alpha\,(\mathbf{b}^T\mathbf{x}))$ for a fixed vector $\mathbf{b}$ and positive scalar α. This test function has the form of (5). However, as α increases, more

[2] $\mathcal{O}(m)$ points in m dimensions is very sparse for $m > 2$.

samples are needed for the computed $\mathbf{w}$ to match $\mathbf{b}$. Second, $f(\mathbf{x})$ might be a symmetric about $\mathbf{w}^T\mathbf{x} = 0$. For example, if $f(\mathbf{x}) = (\mathbf{b}^T\mathbf{x})^2$ for a fixed vector $\mathbf{b}$, then Algorithm 1's $\mathbf{w}$ will not produce a summary plot that reveals the one-dimensional structure in f. Third, $f(\mathbf{x})$ may change significantly as $\mathbf{x}$ is varied along more than one direction. When gradients are available, the eigenvalues of $\boldsymbol{C}$ from (1) can distinguish between the first two cases and the third case. However, using only Algorithm 1, it is not possible to distinguish between these cases.

3 Application to a Li battery model

We apply the active subspace-based techniques to a data set derived from a numerical simulation of a Li battery model described by Hadigol *et al.* (2015), who developed the simulation for an uncertainty quantification study. We briefly summarize the most important aspects of this model for our purposes, and we refer the interested reader to Hadigol *et al.* (2015) for details and references that provide context in the battery modeling literature.

Newman's model (Newman and Tiedemann, 1975) is a coupled system of nonlinear differential equations that describes a Li battery cell as an *anode* and *cathode* separated by a *separator*. As the cell discharges, Li^+ ions diffuse from anode to cathode through the separator, and electrons flow through the external circuit from the negatively charged electrode (the anode) to the positively charged electrode (the cathode). The flow of electrons creates electrical current that powers an electronic device. Newman's model includes several parameters that characterize the physical processes and material properties affecting the cell's power generation. For our purposes, we identify the model's output quantities of interest and its inputs, and we apply the active subspace-based techniques to study the input/output relationships. In the notation of the previous section, the outputs are f and the inputs are $\mathbf{x}$.

3.1 Output quantities of interest

A battery designer may use several model outputs as quantities of interest to characterize performance. For demonstration, we consider two quantities of interest: (i) capacity as a function of voltage and (ii) voltage as a function of time. Capacity is the available energy stored in a fully charged battery measured in milliampere-hours per square centimeter ($\text{mAh} \cdot \text{cm}^{-2}$), and is inversely proportional to the cell voltage. The battery's voltage—measured in volts (V)—decreases as the battery discharges; we study the voltage over the discharge process.

3.2 Input parameters

Hadigol *et al.* (2015) modeled 19 of the Newman model's input parameters as random variables to study the effects of input uncertainties on output quantities of interest (including capacity and voltage). They repeat this study for three different discharge rates: 0.25C, 1C, and 4C, where C denotes the so-called C-rate measuring the rate at which a battery discharges from its full capacity (Pistoia, 2013, Chapter 7). Realistically, when a battery is connected to an electronic device, its discharge rate is not constant; the rate depends on the device's consumption. Studying three different constant rates allows Hadigol *et al.* (2015) to observe how the uncertainty quantification changes, globally, with the discharge rate. The data set for the present study is similar.

Table 1 summarizes the battery model parameters and their associated distributions from Hadigol *et al.* (2015). These parameter distributions were taken from the available modeling literature for $LiC_6/LiCoO_2$ cells. In some cases, characterizations of the parameters' variability is not available in the literature, so Hadigol *et al.* (2015) made modeling choices consistent with engineering expertise. Short descriptions of each parameter follow. Additionally, when available, we provide an engineer's intuition on how changes in the parameter affect the quantity of interest.

3.2.1 Porosity, ϵ

Porosity is the ratio of pore volume to bulk volume. Each component of the cell model—anode, cathode, and separator—has its own porosity parameter: ϵ_a, ϵ_c, and ϵ_s. Increasing

Table 1: Units, notation, and distributions for the parameters $\mathbf{x}$ of the battery model. The distributions from Hadigol *et al.* (2015) represent a particular set of operating conditions for a $LiC_6/LiCoO_2$ cell.

Name	Units	Notation	Nominal	Distribution
anode porosity	—	ϵ_a	0.485	$U[0.46, 0.51]$
anode Bruggeman coeff.	—	brugg_a	4	$U[3.8, 4.2]$
anode solid diffusion coeff.	$\text{m}^2\,\text{s}^{-1}$	$D_{s,a}$	3.9×10^{-14}	$U[3.51, 4.29] \times 10^{-14}$
anode conductivity	$\text{S}\,\text{m}^{-1}$	σ_a	100	$U[90, 110]$
anode reaction rate	$\text{m}^4\,\text{mol}\,\text{s}$	k_a	5.031×10^{-11}	$U[4.52, 5.53] \times 10^{-11}$
anode partical size	μm	$r_{s,a}$	2	$N(2, 0.1354)$
anode length	μm	L_a	80	$U[77, 83]$
cathode porosity	—	ϵ_c	0.385	$U[0.36, 0.41]$
cathode Bruggeman coeff.	—	brugg_c	4	$U[3.8, 4.2]$
cathode solid diffusion coeff.	$\text{m}^2\,\text{s}^{-1}$	$D_{s,c}$	1.0×10^{-14}	$U[0.90, 1.10] \times 10^{-14}$
cathode conductivity	$\text{S}\,\text{m}^{-1}$	σ_c	100	$U[90, 110]$
cathode reaction rate	$\text{m}^4\,\text{mol}\,\text{s}$	k_c	2.334×10^{-11}	$U[2.10, 2.56] \times 10^{-11}$
cathode partical size	μm	$r_{s,c}$	2	$N(2, 0.3896)$
cathode length	μm	L_c	88	$U[85, 91]$
separator porosity	—	ϵ_s	0.724	$U[0.63, 0.81]$
separator Bruggeman coeff.	—	brugg_s	4	$U[3.2, 4.8]$
separator length	μm	L_s	25	$U[22, 28]$
Li^+ transference number	—	t_+^0	0.363	$U[0.345, 0.381]$
salt diffusion coeff. in liquid	$\text{m}^2\,\text{s}^{-1}$	D	7.5×10^{-10}	$U[6.75, 8.25] \times 10^{-10}$

porosity in any component increases power and lowers capacity.

3.2.2 Solid particle size, r

The flux of Li^+ ions is affected by the surface area of the solid particles in the anode and cathode; a larger surface area permits faster reaction. Therefore, a larger particle size—where all particles are modeled as spheres—leads to higher power. One parameter controls the average particle size for each electrode: r_a for the anode and r_c for the cathode.

3.2.3 Bruggeman coefficient, brugg

Bulk transport properties in the cell (e.g., bulk ion transport and diffusion) are affected by a geometric property of the particles called *tortuosity*, τ. The Bruggeman relation expresses tortuosity as porosity raised to a power, $\tau = \epsilon^{(1-\text{brugg})}$, where brugg is the Bruggeman coefficient. Roughly, the smaller the Bruggeman coefficient, the faster the transport and higher the power. Each component of the cell has its own Bruggeman coefficient.

3.2.4 Salt diffusion coefficient, D

The salt diffusion coefficient D is a bulk measure of friction between ions and solvents. As salt diffuses, ions travel more freely. Thus, larger D produces higher power. There is one salt diffusion coefficient for the model.

3.2.5 Solid diffusion coefficient, D_a and D_c

The solid diffusion coefficient characterizes how quickly ions diffuse from the particles in the electrodes, so larger diffusion coefficient leads to higher voltage. The diffusion coefficient for the anode is D_a, and the diffusion coefficient for the cathode is D_c.

3.2.6 Solid conductivity, σ

Increasing conductivity in the electrodes increases power. The anode's conductivity is σ_a, and the cathode's conductivity is σ_c.

3.2.7 Reaction rate, k

Faster chemical reactions—corresponding to higher rate constants—are preferred for Li batteries. The anode's reaction rate is k_a, and the cathode's reaction rate is k_c.

3.2.8 Component length, L

We treat the length of each component as an independent parameter that can vary in the prescribed range. The component lengths are denoted L_a, L_s, and L_c for anode, separator, and cathode, respectively.

4 Data set and results

The data set we use includes input/output pairs for 3600 runs of the simulation model for each of the three discharge rates for a total of 10800 runs. These runs were executed by Hadigol *et al.* (2015) for the uncertainty quantification study. The total set of runs creates approximately 67MB of text data. Each run uses a realization of the input parameters drawn independently according the distributions in Table 1. Given a realization of the inputs, a finite difference method approximates the solution to the system of transport equations that comprises Newman's model. The spatial and temporal discretizations are chosen such that PDE approximation errors are negligible for all parameter values. Each simulation produces (i) 50 voltage/capacity pairs and (ii) 50 time/voltage pairs; the collected pairs from all simulations produce the quantities of interest.

Given initial conditions, each simulation was run until the voltage reached a cutoff of 2.8V. However, the time to reach the threshold depends on the input parameters. Instead of comparing voltage at the same physical time, following Hadigol *et al.* (2015), we introduce a scaled time coordinate that depends on the time to reach the 2.8V threshold. Define $t^* = 100$ at physical time $t = 0$, and let $t^* = 0$ at the physical time when the voltage reaches 2.8V. In effect, t^* represents a charge meter from 100 to 0 for each run. We compare voltages at different parameter values for the same scaled time coordinate t^*.

The input parameters for the simulation were sampled according to the distributions in Table 1. However, for the active subspace-based analysis, we shift and scale the inputs

to the hypercube $[-1, 1]^{19}$. The analysis proceeds on the normalized inputs, which, as in Section 2, we denote $\mathbf{x}$.

The simulation models were run in parallel on the University of Colorado Boulder's JANUS supercomputer. Each run took approximately 20 minutes on 1 core. The total computing time to generate the data was 3600 CPU hours. We developed and executed Python scripts to compute the active subspace weights and produce summary plots. The time to generate these analyses was negligible relative to the computing time used to run the simulations. We executed these scripts on a dual core MacBook Pro with 16GB of memory. The data set and scripts to generate the plots are available at https://bitbucket.org/paulcon/time-dependent-gsa-for-batteries.

4.1 Active subspace results

As described in Section 2.2, we apply Algorithm 1 at each discharge rate (0.25C, 1C, 4C), at each of the 50 voltage values for capacity, and at each of the 50 t^* values for the voltage history. Each application uses all 3600 evaluations. In other words, for the least squares problem (8), $N = 3600$. This is more than sufficient to estimate the 20 coefficients of the linear model. The resulting vector $\mathbf{w}$ has 19 components—the last 19 of the 20 linear model coefficients, normalized as in (9). The summary plots also use all 3600 runs. We stress that these results are for (i) the particular model used to the generate the data set and (ii) the assumptions on parameter variability from Table 1. Strictly speaking, changing any of these assumptions would require a fresh analysis. However, an experienced battery designer may derive insights into other cases and conditions from these results; we do not attempt such extrapolation.

Figures 2, 3, and 4 show the results for capacity as a function of voltage. In each figure, the top subfigure shows $\mathbf{w}$'s components at each of the 50 voltage values. Each component corresponds to one of the 19 model input parameters; the legends to the right match the input parameter with its line style in the plot. For parameter names and units, refer to Table 1. Three gray shaded regions labeled A, B, and C identify three voltages of interest, chosen according to interesting features in the voltage/capacity weights relationships. The middle row of subfigures shows summary plots corresponding to the voltages A, B, and C,

from left to right. The vertical axis scale is chosen to contain all capacity values in the set of simulations at the particular discharge rate. For a particular voltage (A, B, or C), the summary plot shows the relationship between the linear combination of normalized inputs $\mathbf{w}^T\mathbf{x}$ and the capacity. The bottom row of subfigures is identical to the middle row except that the vertical scale is reduced (i.e., zoomed in) to elucidate the relationship between $\mathbf{w}^T\mathbf{x}$ and capacity.

In all cases, the summary plots reveal a relationship between the linear combination of normalized inputs $\mathbf{w}^T\mathbf{x}$ and the capacity. The degree of spread around a univariate functional relationship varies. Figure 2g, which shows results for discharge rate 0.25C and voltage 3.1V, has the tightest univariate relationship; moreover, the relationship is linear. For this case, we are confident that capacity can be well approximated as $c_0 + c_1(\mathbf{w}^T\mathbf{x})$, for some coefficients c_0 and c_1. For this case, all weights are nearly zero except for the weight associated with anode porosity and the weight associated with anode Bruggeman coefficient. Figure 3f, which shows discharge rate 1C at voltage 3.2V, has the largest spread around a univariate functional relationship. A global trend is apparent—and such a trend may be useful for a modeler seeking the range of capacities over the parameter values—but we are much less confident that a function of the form $g(\mathbf{w}^T\mathbf{x})$, where g is a univariate, scalar-valued function, is an appropriate approximation. Broadly, a univariate approximation appears more appropriate for (i) all voltages with discharge rate 4C and (ii) voltages near the ends of voltage range for discharge rates 0.25C and 1C. For intermediate voltages, the relationship between normalized inputs $\mathbf{x}$ and capacity appears more complex than can be captured in the one-dimensional summary plot. The relationship may be well approximated by a function of fewer than m linear combinations of inputs. However, to use active subspaces, we would need to estimate gradients of capacity with respect to $\mathbf{x}$.

When the summary plot reveals a nearly univariate functional relationship, the components of $\mathbf{w}$ can be treated as global sensitivity metrics for the input parameters with respect to the quantity of interest. In fact, their computation is similar to the regression coefficients proposed by Saltelli *et al.* (2008, Chapter 1.2.5) except for the normalization; however, our interpretation is dramatically different. In contrast to the Sobol total sensitivity indices used by Hadigol *et al.* (2015), the components of $\mathbf{w}$ are signed, and the signs

can reveal useful insights into the input/output relationship. Consider univariate relationship revealed in Figure 2g, and note that the relationship is monotonic, i.e., increasing $\mathbf{w}^T\mathbf{x}$ increases capacity. The sign of $\mathbf{w}$'s component associated with anode porosity ϵ_a is positive. Therefore, increasing ϵ_a increases capacity. By similar reasoning, the sign of $\mathbf{w}$'s component associated with the anode Bruggeman coefficient brugg_a is negative, so increasing brugg_a will decrease capacity. The rate of increase or decrease is related to the components' magnitudes.

Treating $\mathbf{w}$'s components as sensitivity metrics, we observe several interesting qualities of the simulation outputs.

- Most of the 19 parameters are relatively unimportant in characterizing the relationship between inputs and capacity. This is consistent with the Sobol index results from Hadigol *et al.* (2015).

- For discharge rate 0.25C, a transition occurs in the parameter sensitivities around 3.7V. At lower voltages, the relationship between inputs and capacity involves only two parameters. At higher voltages, the relationship is still close to linear, but the number of parameters defining the linear relationship is larger.

- The $\mathbf{w}$ component associated with the anode Bruggeman coefficient changes sign as voltage decreases. Coupled with the summary plots, this implies that increasing brugg_a affects capacity in opposite directions, depending on voltage.

- For discharge rate 4C, the sensitivities for porosities and Bruggeman coefficients are roughly opposite. This suggests a trade-off that a battery designer may exploit.

Figures 5, 6, and 7 show results for voltage over the discharge history, i.e., as a function of the scaled time t^*, for the three discharge rates. The format of the figures is identical to the figures for capacity. Compared to capacity, the relationship between the inputs and voltage is better modeled by a univariate function of $\mathbf{w}^T\mathbf{x}$ across the discharge rates and chosen t^* values. Additionally, the sensitivities are less variable as functions of t^* than the capacity sensitivities as a function of voltage.

These figures suggest the following insights into the model.

- Most model parameters are not important when defining the important direction identified by Algorithm 1. Generally, porosities and Bruggeman coefficients are among the most important parameters. This is consistent with the results from Hadigol *et al.* (2015).

- For discharge rate 0.25C, the sizes of electrodes are important. This importance decreases as the discharge rate increases.

- The picture for the highest discharge rate 4C is different from the others. The separator's porosity is by far the most important parameter. As the discharge process progresses, the salt diffusion coefficient suddenly becomes important; this is the only time a diffusion coefficient is important.

Figure 8 shows the bootstrap standard errors on the components of $\mathbf{w}$, where the standard errors are computed with 100 bootstrap replicates from the data set of 3600 runs. We stress that the bootstrap standard errors do not have the proper statistical interpretation, since there is no noise in the data. However, large bootstrap standard error does correspond to activity in the components of $\mathbf{w}$ as a function of their independent coordinate (voltage or t^*). This provides an indication of how the components of $\mathbf{w}$ vary over the bootstrap replicates. Low errors suggest the coefficients are stable with respect to resampling (with replacement) from the data set. Notably, the regions of relatively large bootstrap error—region B in Figures 8a and 8c—correspond to summary plots that have the largest spread around a univariate functional relationship, i.e., where a one-dimensional ridge approximation is least appropriate. This connection is very intriguing, and we expect to explore this connection beyond the Li battery application in future work.

5 Summary and conclusions

Active subspaces are part of an emerging set of tools for discovering and exploiting a particular type of low-dimensional structure in functions of several variables. In particular, given (i) a scalar-valued function $f : \mathbb{R}^m \to \mathbb{R}$ and (ii) a probability density function associated with the function's inputs, the active subspace is defined by the n-dimensional

eigenspace, with $n < m$, of a matrix-valued functional of f's gradient. When gradients are not available, one may approximate the one-dimensional active subspace by identifying the constant gradient of a least-squares fit linear approximation of $f(\mathbf{x})$. In this paper, we extended this idea to functions that also depend on another independent variable, such as time.

We applied this approach to a set of 3600 input/output pairs from three varieties of a simulated lithium battery's discharge process, where each variety uses a different constant discharge rate. The model contained 19 input parameters, and we examined two output quantities: (i) capacity as a function of voltage and (ii) voltage as a function of time. In every case, there exists a one-dimensional active subspace in the 19-dimensional parameter space, though output variation orthogonal to the active direction changes across output quantities. Therefore, the components of the vector that defines the active subspace can be used as sensitivity metrics for the 19 parameters. The components' behavior over the independent coordinate (voltage or time, respectively) reveals stages of activity in the output quantities.

A gradient-based study may reveal higher dimensional structure in regions where the one-dimensional model—based on the least-squares linear approximation—is insufficient to characterize the input/output map. Future work may seek a simulation model with such gradient capabilities.

References

Blatman, G. and Sudret, B. (2011). Adaptive sparse polynomial chaos expansion based on least angle regression. *Journal of Computational Physics*, **230**, 2345–2367.

Constantine, P. (2015). *Active Subspaces: Emerging Ideas in Dimension Reduction for Parameter Studies*. SIAM, Philadelphia.

Constantine, P. and Gleich, D. (2015). Computing active subspaces with Monte Carlo. *arXiv preprint arXiv:1408.0545v2*.

Constantine, P., Dow, E., and Wang, Q. (2014). Active subspace methods in theory and

practice: Applications to kriging surfaces. *SIAM Journal on Scientific Computing*, **36**(4), A1500–A1524.

Constantine, P., Zaharatos, B., and Campanelli, M. (2015a). Discovering an active subspace in a single-diode solar cell model. *Statistical Analysis and Data Mining: The ASA Data Science Journal*, pages n/a–n/a.

Constantine, P., Emory, M., Larsson, J., and Iaccarino, G. (2015b). Exploiting active subspaces to quantify uncertainty in the numerical simulation of the HyShot II scramjet. *Journal of Computational Physics*, **302**, 1–20.

Cook, R. D. (1998). *Regression graphics: Ideas for studying regressions through graphics*. John Wiley & Sons.

Diaz, P. and Constantine, P. G. (2015). Global sensitivity metrics from active subspaces. *arXiv:1510.04361*.

Doherty, C. M., Caruso, R. A., and Drummond, C. J. (2010). High performance lifepo 4 electrode materials: influence of colloidal particle morphology and porosity on lithium-ion battery power capability. *Energy & Environmental Science*, **3**(6), 813–823.

Doostan, A. and Iaccarino, G. (2009). A least-squares approximation of partial differential equations with high-dimensional random inputs. *Journal of Computational Physics*, **228**(12), 4332–4345.

Doostan, A. and Owhadi, H. (2011). A non-adapted sparse approximation of PDEs with stochastic inputs. *Journal of Computational Physics*, **230**, 3015–3034.

Doostan, A., Iaccarino, G., and Etemadi, N. (2007). A least-squares approximation of high-dimensional uncertain systems. Technical Report Annual Research Brief, Center for Turbulence Research, Stanford University.

Doyle, M., Fuller, T., and Newman, J. (1993). Modeling of galvanostatic charge and discharge of the lithium/polymer/insertion cell. *Journal of the Electrochemical Society*, **140**(6), 1526–1533.

Dua, W., Gupta, A., Zhang, X., Sastry, A. M., and Shyy, W. (2010). Effect of cycling rate, particle size and transport properties on Lithium-ion cathode performance. *International Journal of Heat and Mass Transfer*, **53**, 3552–3561.

Efron, B. and Tibshirani, R. J. (1994). *An Introduction to the Bootstrap*. CRC press.

Griewank, A. (2000). *Evaluating Derivatives: Principles and Techniques of Algorithmic Differentiation*. SIAM, Philadelphia.

Hadigol, M., Doostan, A., Matthies, H., and Niekamp, R. (2014). Partitioned treatment of uncertainty in coupled domain problems: A separated representation approach. *Computer Methods in Applied Mechanics and Engineering*, **274**, 103–124.

Hadigol, M., Maute, K., and Doostan, A. (2015). On uncertainty quantification of lithium-ion batteries: Application to an LiC6/LiCoO2 cell. *Journal of Power Sources*, **300**, 507–524.

Hampton, J. and Doostan, A. (2015a). Coherence motivated sampling and convergence analysis of least squares polynomial chaos regression. *Computer Methods in Applied Mechanics and Engineering*, **290**, 73 – 97.

Hampton, J. and Doostan, A. (2015b). Compressive sampling of polynomial chaos expansions: Convergence analysis and sampling strategies. *Journal of Computational Physics*, **280**, 363 – 386.

Hampton, J. and Doostan, A. (2016). *Compressive Sampling Methods for Sparse Polynomial Chaos Expansions*, pages 1–29. Springer International Publishing.

Kato, T. (1966). *Perturbation Theory for Linear Operators*. Springer Science+Business Media, New York.

Li, K.-C. and Duan, N. (1989). Regression analysis under link violation. *The Annals of Statistics*, **17**(3), 1009–1052.

Loudon, T. and Pankavich, S. (2016). Mathematical analysis and dynamic active subspaces for a long term model of HIV. *arXiv:1604.04588*.

Mathelin, L. and Gallivan, K. (2012). A compressed sensing approach for partial differential equations with random input data. *Commun. Comput. Phys.*, **12**, 919–954.

Matthies, H. and Zander, E. (2012). Solving stochastic systems with low-rank tensor compression. *Linear Algebra and its Applications*, **436**(10), 3819–3838.

Newman, J. and Tiedemann, W. (1975). Porous-electrode theory with battery applications. *AIChE Journal*, **21**(1), 25–41.

Nouy, A. (2010). Proper generalized decompositions and separated representations for the numerical solution of high dimensional stochastic problems. *Archives of Computational Methods in Engineering*, **17**, 403–434.

Pinkus, A. (2015). *Ridge Functions*. Cambridge University Press, Cambridge.

Pistoia, G. (2013). *Lithium-ion batteries: advances and applications*. Newnes.

Saltelli, A., Ratto, M., Andres, T., Campolongo, F., Cariboni, J., Gatelli, D., Saisana, M., and Tarantola, S. (2008). *Global sensitivity analysis: the primer*. John Wiley & Sons.

Santhanagopalan, S. and White, R. E. (2007). Modeling parametric uncertainty using polynomial chaos theory. *ECS Trans.*, **3**, 243–256.

Winter, M. and Brodd, R. (2004). What are batteries, fuel cells, and supercapacitors? *Chemical Review*, **104**(10), 4245–4269.

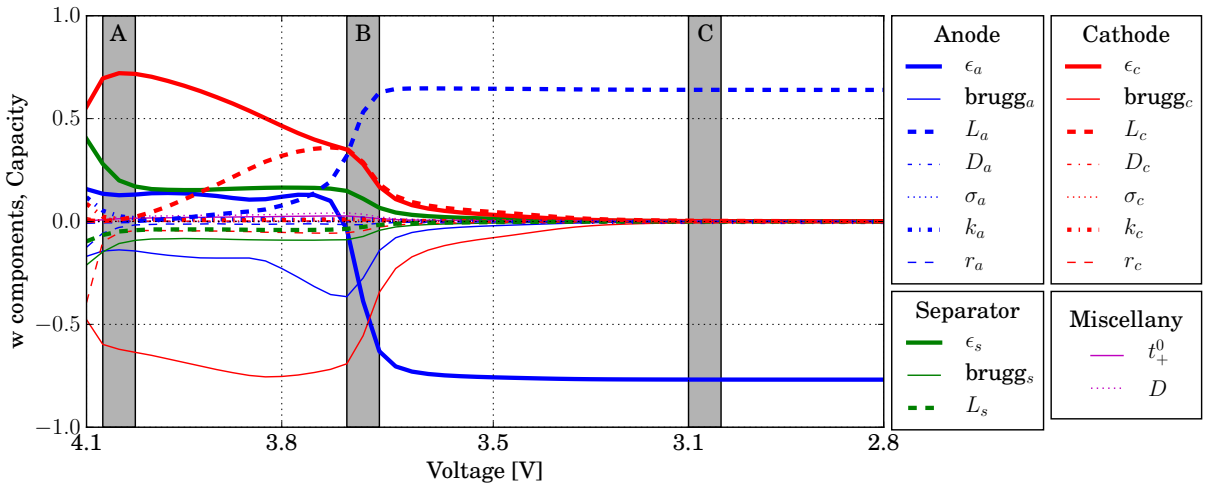

(a) Components of $\mathbf{w}$ from Algorithm 1 as function of voltage

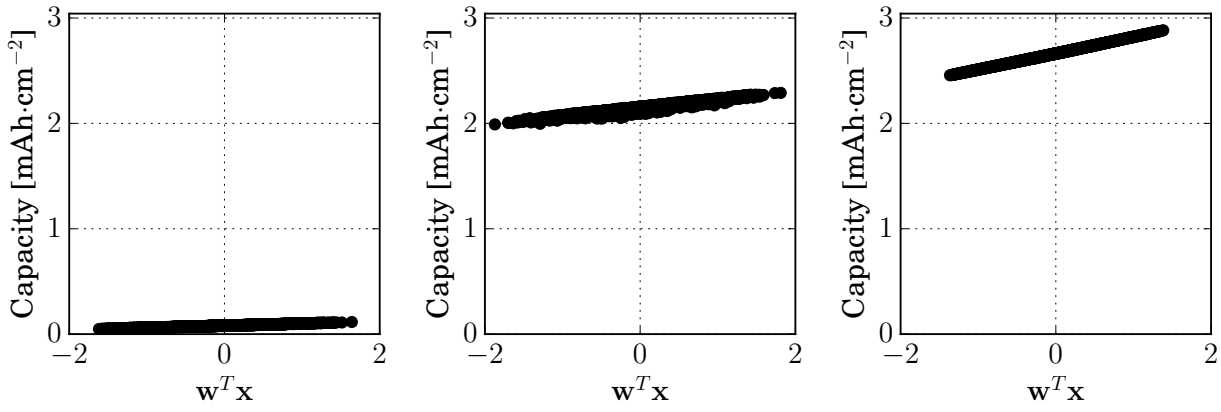

(b) A (4.1V) (c) B (3.7V) (d) C (3.1V)

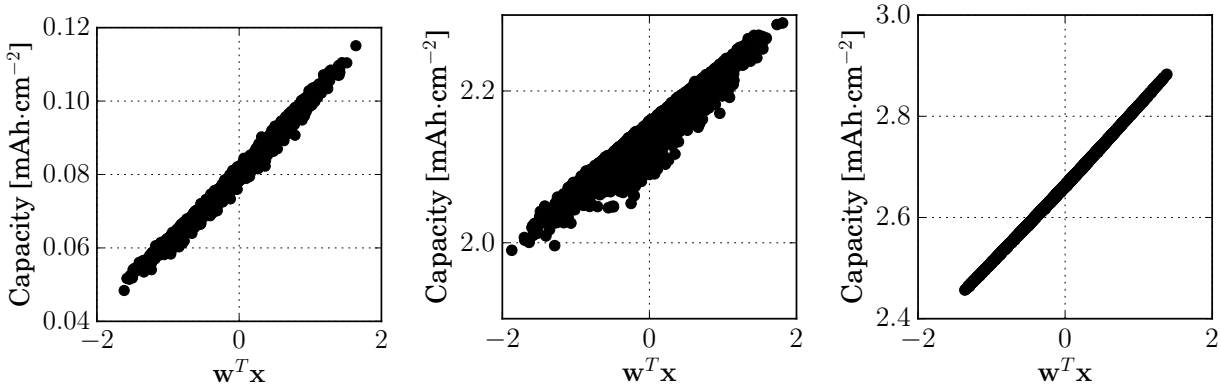

(e) A (4.1V) (f) B (3.7V) (g) C (3.1V)

Figure 2: Results for capacity at discharge rate 0.25C. The top figure shows the components of $\mathbf{w}$ from Algorithm 1 as function of voltage. The middle row shows summary plots corresponding to the voltages labeled A, B, and C in the top figure. The bottom row is identical to the top row with the vertical axis zoomed to elucidate the relationship.

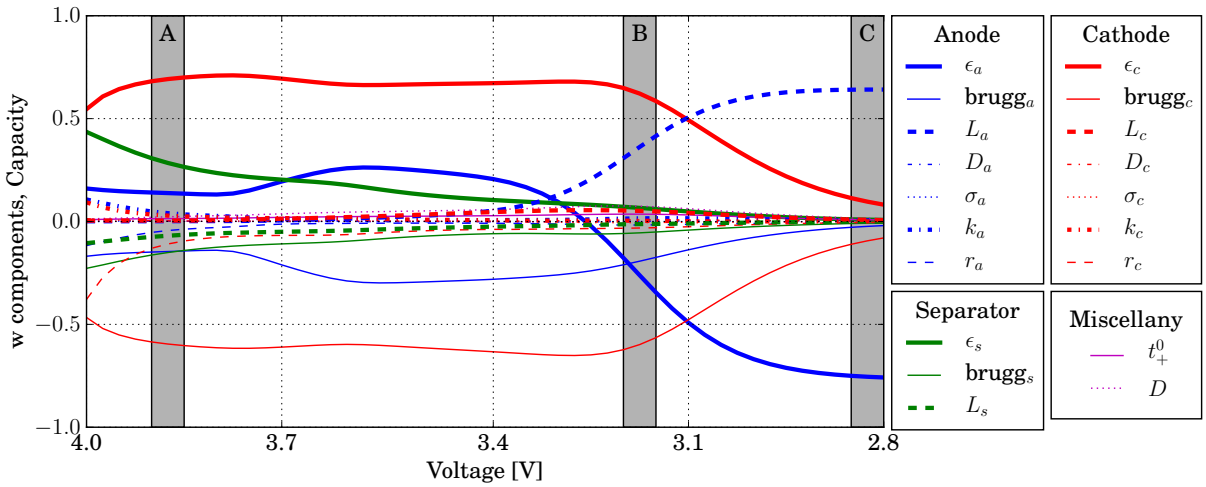

(a) Active subspace weights as function of voltage

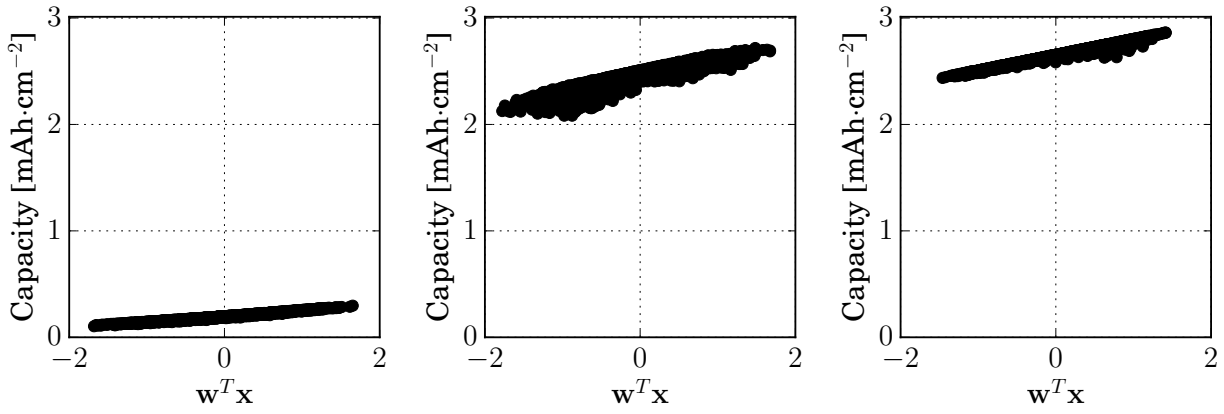

(b) A (3.9V) (c) B (3.2V) (d) C (2.8V)

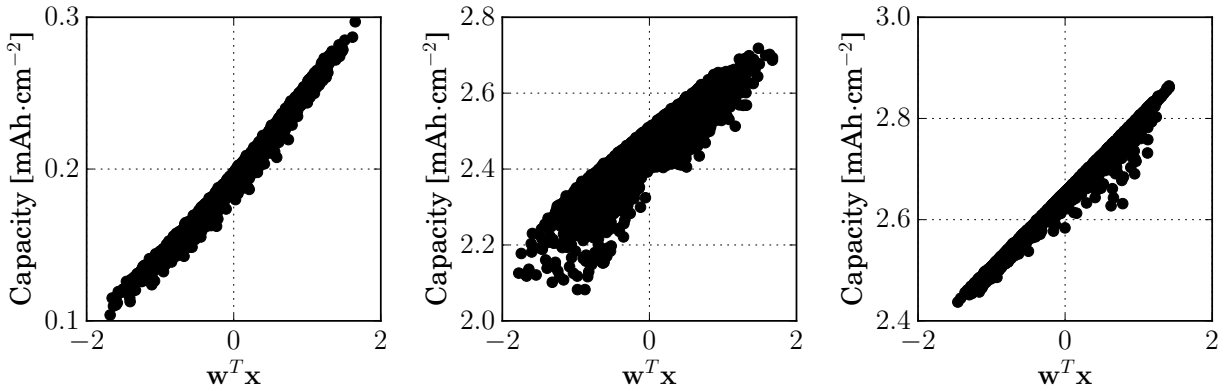

(e) A (3.9V) (f) B (3.2V) (g) C (2.8V)

Figure 3: Results for capacity at discharge rate 1C. The top figure shows the components of $\mathbf{w}$ from Algorithm 1 as function of voltage. The middle row shows summary plots corresponding to the voltages labeled A, B, and C in the top figure. The bottom row is identical to the top row with the vertical axis zoomed to elucidate the relationship.

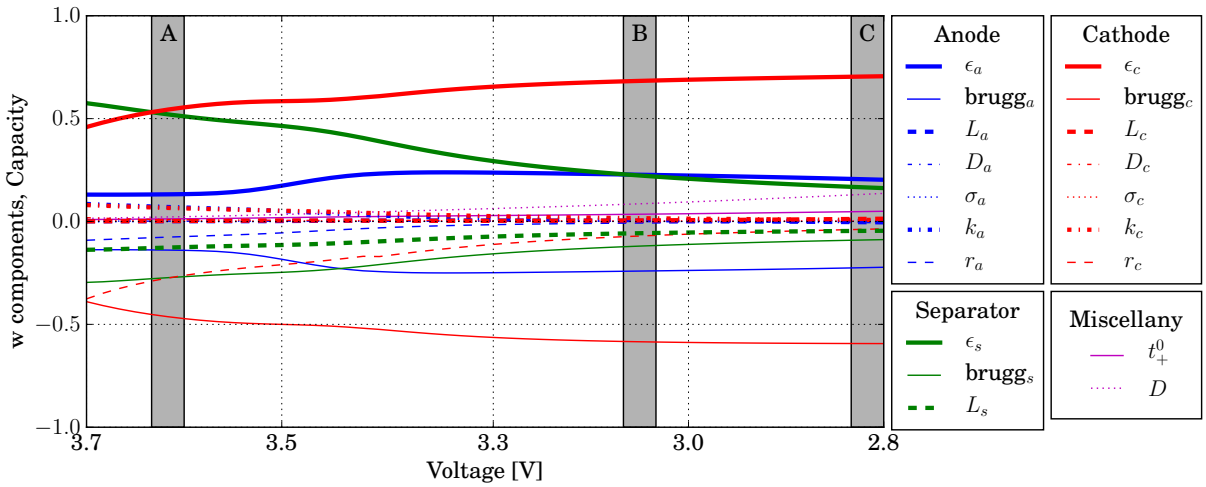

(a) Active subspace weights as function of voltage

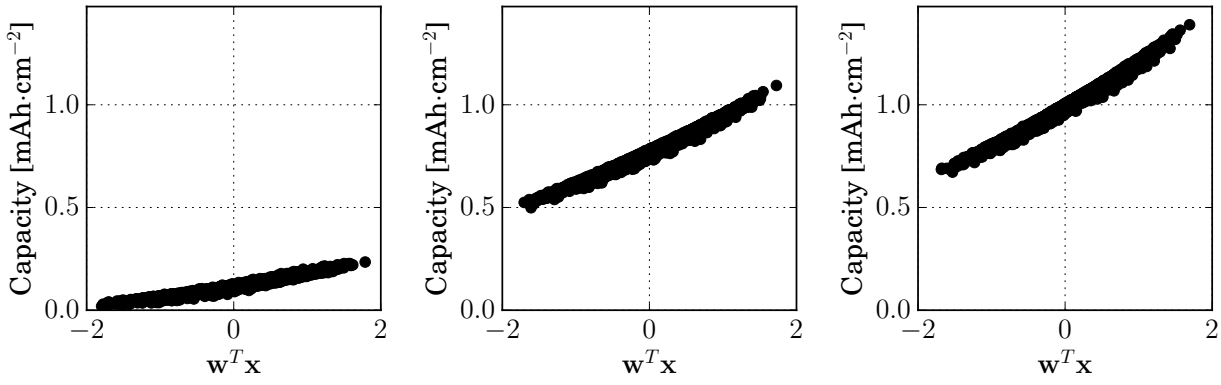

(b) A (3.6V) (c) B (3.1V) (d) C (2.8V)

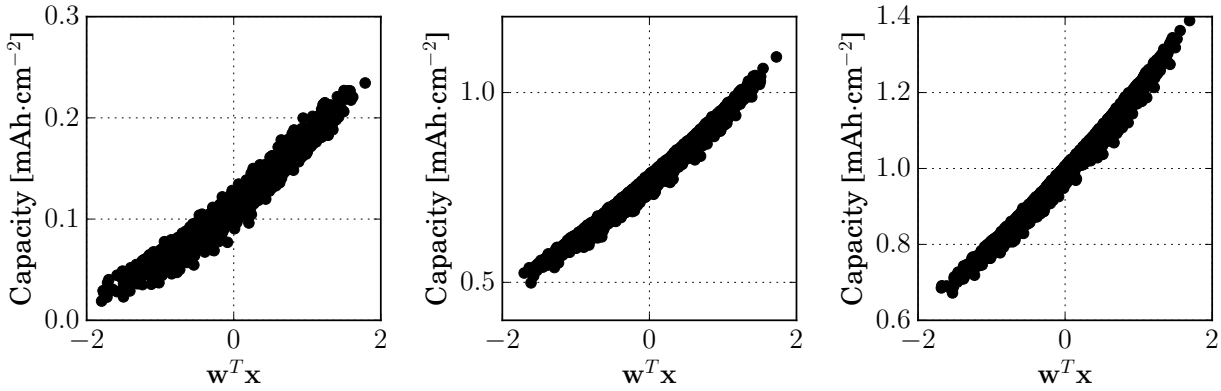

(e) A (3.6V) (f) B (3.1V) (g) C (2.8V)

Figure 4: Results for capacity at discharge rate 4C. The top figure shows the components of $\mathbf{w}$ from Algorithm 1 as function of voltage. The middle row shows summary plots corresponding to the voltages labeled A, B, and C in the top figure. The bottom row is identical to the top row with the vertical axis zoomed to elucidate the relationship.

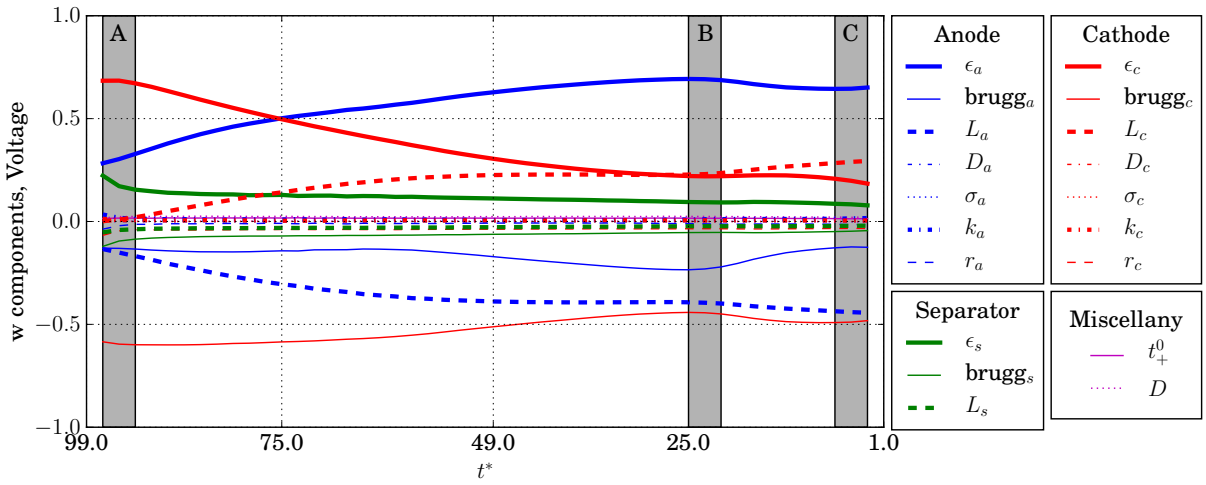

(a) Active subspace weights as function of t^*

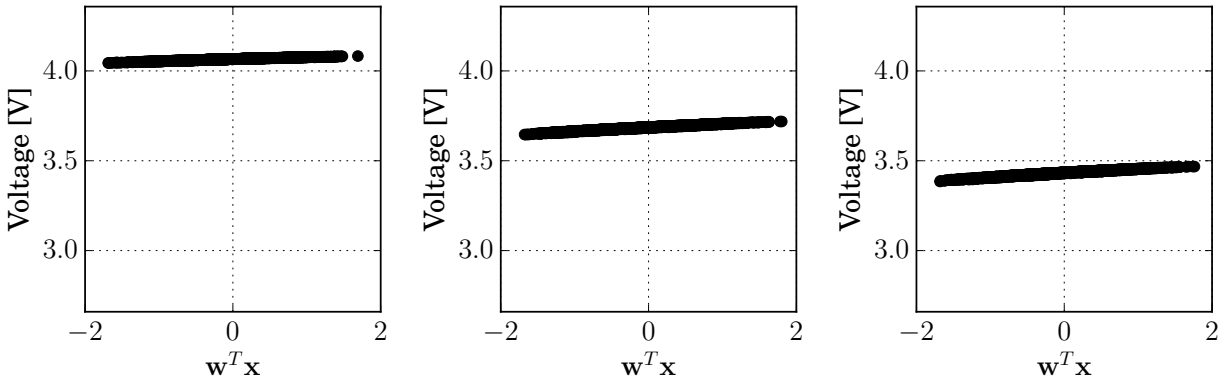

(b) A ($t^* = 95$)

(c) B ($t^* = 23$)

(d) C ($t^* = 5$)

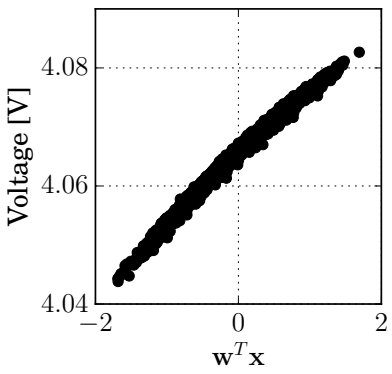

(e) A ($t^* = 95$)

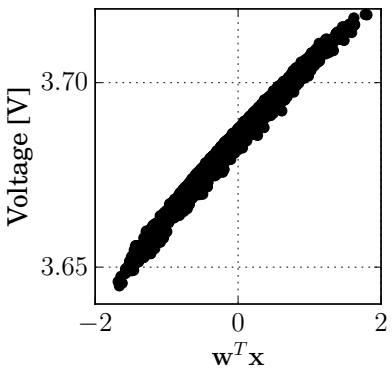

(f) B ($t^* = 23$)

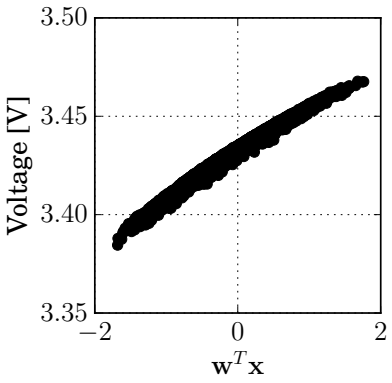

(g) C ($t^* = 5$)

Figure 5: Results for voltage at discharge rate 0.25C. The top figure shows the components of $\mathbf{w}$ from Algorithm 1 as function of t^*. The middle row shows summary plots corresponding to the voltages labeled A, B, and C in the top figure. The bottom row is identical to the top row with the vertical axis zoomed to elucidate the relationship.

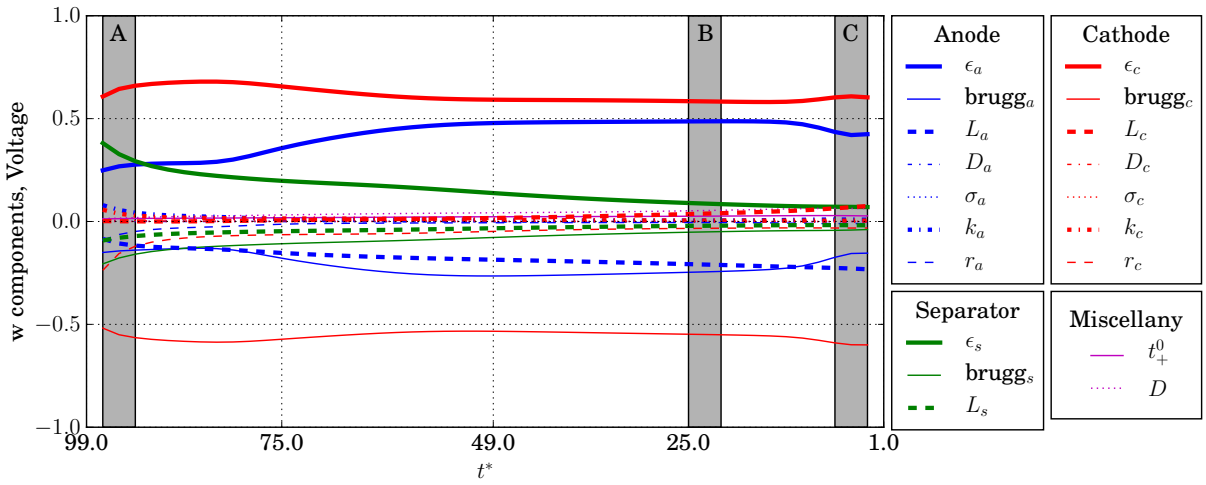

(a) Active subspace weights as function of t^*

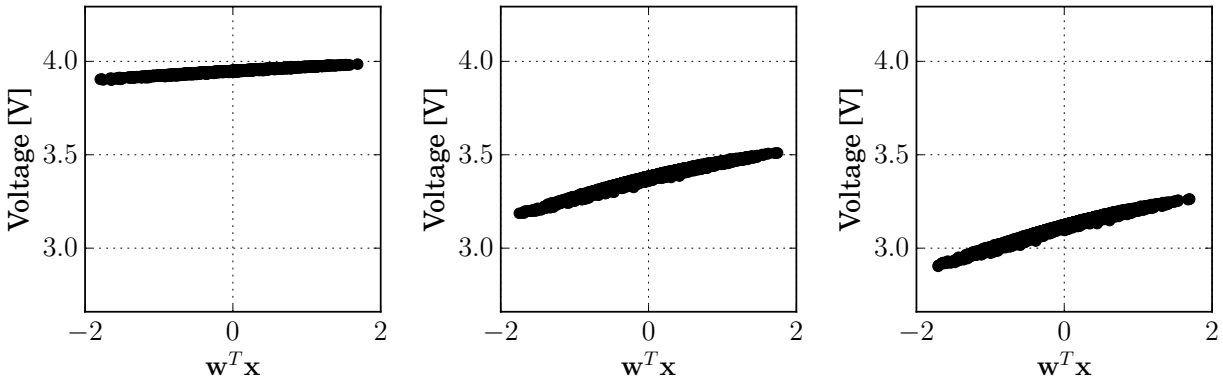

(b) A ($t^* = 95$)

(c) B ($t^* = 23$)

(d) C ($t^* = 5$)

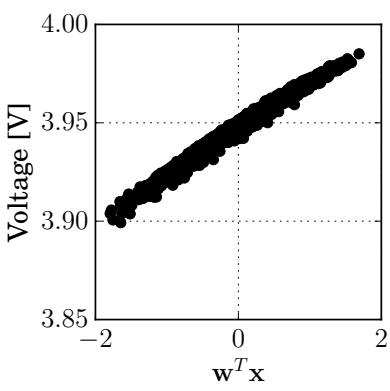

(e) A ($t^* = 95$)

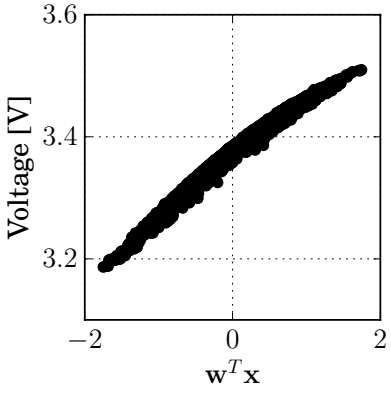

(f) B ($t^* = 23$)

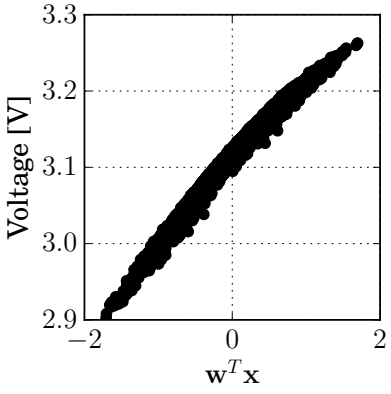

(g) C ($t^* = 5$)

Figure 6: Results for voltage at discharge rate 1C. The top figure shows the components of $\mathbf{w}$ from Algorithm 1 as function of t^*. The middle row shows summary plots corresponding to the voltages labeled A, B, and C in the top figure. The bottom row is identical to the top row with the vertical axis zoomed to elucidate the relationship.

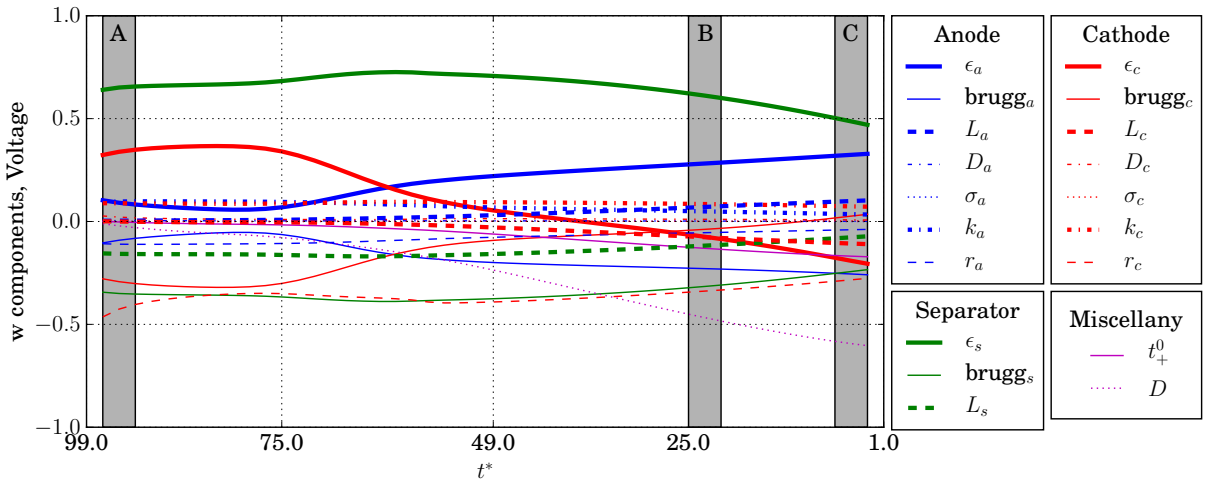

(a) Active subspace weights as function of t^*

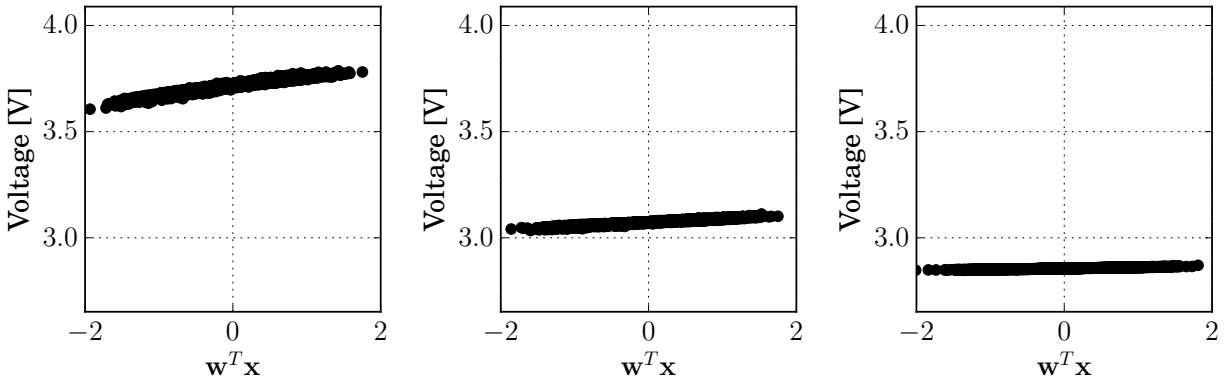

(b) A ($t^* = 95$)

(c) B ($t^* = 23$)

(d) C ($t^* = 5$)

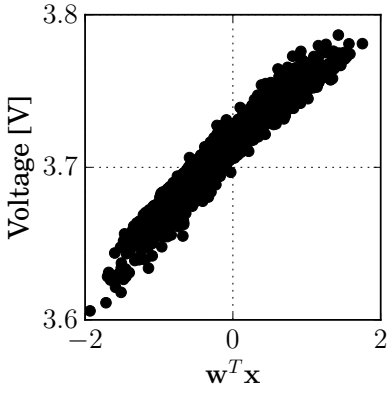

(e) A ($t^* = 95$)

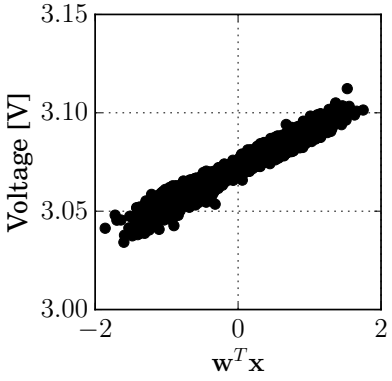

(f) B ($t^* = 23$)

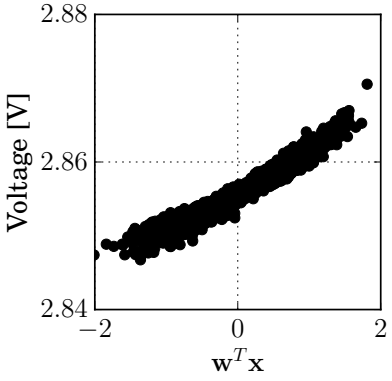

(g) C ($t^* = 5$)

Figure 7: Results for voltage at discharge rate 4C. The top figure shows the components of $\mathbf{w}$ from Algorithm 1 as function of t^*. The middle row shows summary plots corresponding to the voltages labeled A, B, and C in the top figure. The bottom row is identical to the top row with the vertical axis zoomed to elucidate the relationship.

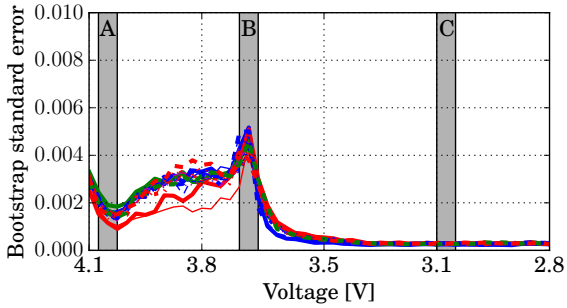

(a) Capacity, $I = 0.25C$

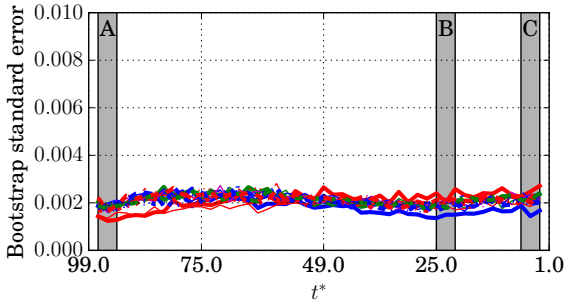

(b) Voltage, $I = 0.25C$

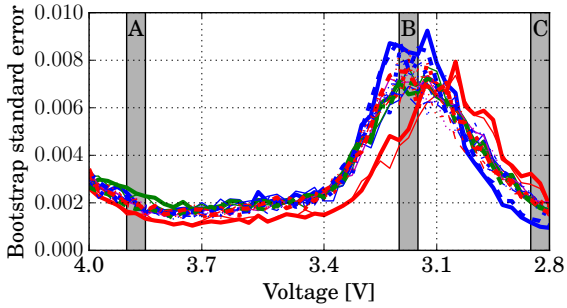

(c) Capacity, $I = 1C$

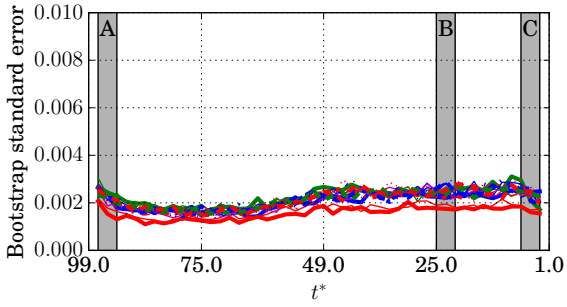

(d) Voltage, $I = 1C$

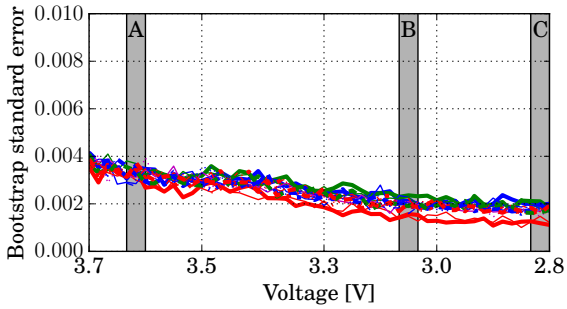

(e) Capacity, $I = 4C$

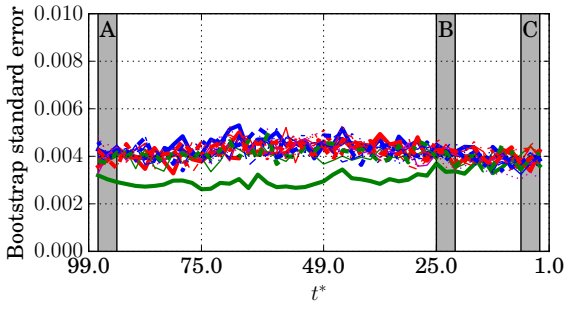

(f) Voltage, $I = 4C$

Figure 8: Bootstrap standard errors for the components of $\mathbf{w}$. Figures 8a, 8c, and 8e are for capacity as a function of voltage; see Figures 2, 3, and 4, respectively. Figures 8b, 8d, and 8f are for voltage over the discharge process; see Figures 5, 6, and 7, respectively.